Quality Detection of Common Beans Flour Using Hyperspectral Imaging Technology: Potential of Machine Learning and Deep Learning.

RASHVAND, Mahdi, PATERNA, Giuliana, LAVEGLIA, Sabina, ZHANG, Hongwei <http://orcid.org/0000-0002-7718-021X>, SHENFIELD, Alex <http://orcid.org/0000-0002-2931-8077>, GIOIA, Tania, ALTIERI, Giuseppe, DI RENZO, Giovanni Carlo and GENOVESE, Francesco

Quality Detection of Common Beans Flour Using Hyperspectral Imaging Technology: Potential of Machine Learning and Deep Learning

Mahdi Rashvand [a,b*], Giuliana Paterna [b], Sabina Laveglia [b], Hongwei Zhang [a], Alex Shenfield [a], Tania Gioia [b], Giuseppe Altieri [b], Giovanni Carlo Di Renzo [b], Francesco Genovese [b]

[a] National Centre of Excellence for Food Engineering, Sheffield Hallam University, Sheffield, UK

[b] DAFE, Department of Agricultural, Forestry, Food and Environmental Sciences, University of Basilicata, Potenza, Italy

* Corresponding author: M.Rashvand@shu.ac.uk

Abstract:

Carbohydrate content is one of the most crucial factors in common beans flour (CBF) quality after processing. However, the analysis procedure necessitates the time-consuming and costly selection of elite genotypes from many experimental lines in a destructive manner. Combining hyperspectral imaging (HSI) with machine learning (ML) algorithms provides an effective and fast approach for evaluating the quality of food products. This study determined the quality of CBF by evaluating the contents of carbohydrate using HSI technology. The samples of this work were composed of 12 varieties CBF and each variety was treated by hydration-dehydration method. After various spectral preprocessing steps, spectral features were extracted from the spectral profiles using different feature extraction methods. Partial least square regression (PLSR), Support vector machine regression (SVMR) and Temporal convolutional network-attention (TCNA) were established to predict the contents of carbohydrate in CBF. The best value of R2 and the RMSE and RPD were 0.982, 0.165 and 4.905, respectively by topology of OSC-CARS-TCNA. The outputs demonstrated although deep learning presents more accuracy than ML models, the applied ML models not only provided acceptable and reliable accuracy but also affect significantly in time-analyzing. In addition, visualization output of the current research revealed that the developed models and system can integrate to some intelligent sensors for digitalization aims. This study demonstrates the combination of HSI and ML can be an effective tool in improving the CBF processing industry and providing sustainable and efficient methods in the production of CBF.

Key words: Common beans flour, Machine learning, Quality prediction, HSI, Hydration-dehydration treatment

1. Introduction

Common beans are essential to the food system's sustainability because of their multifaceted positive impacts environmentally, economically, and nutritionally. Common beans are essential in richness for proteins, fiber, vitamins, and minerals, thus making critical contributions to dietary requirements, especially in developing countries where sources of proteins are limited (Yu et al., 2022). The annual global production of beans in 2023 was forecasted at 30 million metric tons, with a multifunctional potential for beans that indicates the importance of beans for driving the

sustainable practices of the food industry (FAO, 2023). Bean flour can be produced from the wet-milled or the dry-milled process. The natural thickener capacity of bean flour is utilizable in soups, sauces, and instant meal formulations, adding a creamy texture and enhancing its nutritional value (Alfaro-Diaz et al., 2023). Therefore, diverse bean flour applications are very crucial in the further development of health, sustainability, and innovation in food industry, hence, the producers and processors should heed to the quality of bean flour.

The main critical parameters that influence in a robust way the quality and functionality of ordinary bean flour are variety, processing methods, and environmental factors. The variety of beans is necessary for determining the nutrient composition and its inherent characteristics, such as protein content, fiber levels, and antioxidant properties (Wainaina et al., 2021). Wainaina et al. (2021) and Uebersax et al. (2023) revealed that carbohydrate content has an important role in determining functional properties such as water absorption, viscosity, and textural characteristics in CBF, and thus it holds great importance in food formulations. The increased levels of carbohydrate may enhance the gelation and thickening characteristics of the CBF, thereby improving the nutritional quality of the flour. The diversity of the processes and conditions include drying, milling, and storage, during the processing highly influence the physicochemical properties of bean flours. For instance, the drying temperature and time taken to dry will affect the retention of nutrients and the final moisture content; these will directly affect the shelf life and the susceptibility to microbial contamination (Uebersax et al., 2023). Therefore, there is a need to understand quality that incorporates desired functional and nutritional attributes for the consumption target of bean flour.

Non-destructive methods such as near-infrared spectroscopy (Zaukuu et al., 2024), machine vision (Fdez-Vidal et al., 2024), Fourier transform infrared (Liu et al., 2022), Raman spectroscopy (Sato and Numata, 2024), and hyperspectral imaging (Zhang et al., 2023) have been applied for detection of food quality. Zaukuu et al. (2024) were able to predict protein, carbohydrate, total color change, fat, and lightness precisely in melon seed powders. Sato and Numat. (2024) performed an experiment for simultaneous quantitative analysis of quercetin and rutin in Tartary buckwheat flour using Raman Spectroscopy (RS). Developing a partial least square model, the Raman spectra of quercetin and rutin in ethanol solutions at various concentrations were measured. Both NIR and RS were easy to operate, able to monitor water-rich samples and fingerprint the identification features very well. However, broad overlapping spectra and limited sensitivity for direct detection of trace components cause challenges and limitations for applying the mentioned methods (Ma et al., 2023). Therefore, some researchers have been encouraged to use hyperspectral imaging (HSI) for non-destructive quality evaluation of food.

HSI techniques have been applied in the quality assessment of various flours and powders by simultaneous acquisition of image, spectra and spatial information, enabling the precise assessment of compositional attributes (Saha et al., 2023; Zhang et al., 2023; He et al., 2023; Li et al., 2024). Conventional methods for the analysis of CBF quality generally involve time-consuming and destructive techniques and require an elaborate preparation of samples besides not having spatially resolved data. HSI coupled with ML has been enabled for fast, nondestructive, and high-throughput analysis of these products by capturing their spectral fingerprints related to their compositional properties, hence enabling the prediction of quality parameters with high accuracy and well-resolved spatial information. Zhang et al. (2023) used HSI for rapid determination of protein, starch and moisture content in wheat flour. Further, Li et al.

(2024) applied HSI to predict and visualize matcha color physicochemical indicators. The approach presented in the literature applied to quality control of various powdery foods. However, due to the limited performance of the calibration model and the effect of image noise, they recommended to use multivariate calibration algorithms and optimized machine learning (ML) methods.

The merging of spectroscopy systems with machine learning methods-like support vector regression (Guan et al., 2024), decision trees (Zhao et al., 2024), and artificial neural networks (Jiang et al., 2024) allows for the powerful, complete, precise automation of data analysis from complicated datasets to support a wide range of scientific applications. The combined VIS-NIR Bayesian optimization machine learning algorithm was proposed by Guan et al. (2024). It was applied for fast authentication of Panax notoginseng powder. The results showed that most of the proposed methods gave very good performances in the discriminant analysis of the flour varieties, with deep learning algorithms reaching up to 100 % accuracy during the testing periods. Zhao et al. (2024) employed four algorithms comprising DT, LDA, KNN, and SVM for recognizing lily origins based on HSI. They reported not only that all models had a prediction accuracy above 90.0%, but also the potential capability for reaching 100.0% with optimization of the hyperparameters of an image processing technique. The conclusion is that hyperspectral imaging teamed with machine learning offers enormous possibilities and threats for the fast assessment of fresh food quality, allowing an in-depth analysis of their chemical and physical properties, enhancing quality control, and ensuring the safety of foods.

A critical literature review of the nondestructive ways in food quality evaluation has resulted in techniques such as NIR and traditional machine vision systems when some unique strengths are considered-in particular, either rapid analysis provided, structural insights, or major compositional assessments-but often lack certain comprehensive spatial and spectral information well provided by hyperspectral imagining (Barbedo, 2023). But each of these methods has its own limitation, such as an applicability range, low resolution, or nonsimultaneous assessment ability. HSI is especially suitable here, given its ability for integration of spatial and spectral information into one image, allowing for both high accuracy and multi-parameter investigations of the quality (Ma et al., 2023).

Several works in the literature have reported on the application of HSI systems for quality assessment of flours and flours of various products. However, there is no research (to the best of our knowledge) focusing on potential of HSI and ML to characterization of various untreated/treated common bean flour. Therefore, the main aims of the current paper are i) effect of hydration-dehydration treatments on the physicochemical properties of various common beans; ii) Determine carbohydrates, proteins, fats and starch content in the common beans flour by using traditional chemical methods and obtain HSI images information iii) Using different robust spectral pre-processing and feature extraction; iv) Apply different Ml models consist of partial least square regression (PLSR), support vector machine regression (SVMR), and Temporal convolutional network-attention (TCNA) methods and v) applying the image processing optimal model enables visualization of the chemical composition distribution of all flour beans pixels.

2. Material and methods

2.1. Sample preparation

In the present study, twelve genotypes of common bean (Phaseolus vulgaris L.) from different Mediterranean areas were used: IT-134, IT-206, IT-380, IT-449 and IT-874 (Italy), SP-171 and SP-496 (Spain), GR-430 and GR-833 (Greece), AL-924 and AL-1237 (Albania) and CR-1417 (Croatia). Mature seeds were manually sorted and cleaned to remove foreign material, dirt, dust, damaged and immature grains and stored in a dry environment at room temperature (21 ± 2°C) until further use. For each genotype, beans were divided into two portions identified as were identified as undehulled (or non-treated beans, NT) and dehulled (or pre-treated beans, T). Before dehulling treatment, seeds were soaked for 16 h at room temperature (21 ± 2°C) in distilled water (1:5, w/v, bean to water ratio) and dried in a ventilated drying oven at 60°C for 6 h. Beans were then dehulled using an impact dehuller prototype (Otake FS20, 1850 rpm). Each bean sample was ground to obtain a fine powder using a stainless-steel mill (Thermomix Vorwerk TM31, Wuppertal, Germany) at 10000 rpm and 30 s intervals for a total 3 min milling. All twenty-four samples were collected and stored in polyethylene bags at room temperature until analysis.

2.2. Spectral data acquisition

2.2.1 Hyperspectral imaging

A near-infrared hyperspectral imaging (NIR-HSI) system equipped line-scan spectrograph (Headwall Photonics, Fitchburg, MA, USA) that covers a spectral range of 890-2500 nm has been applied. Two halogen lamps (Ushio EKE, 150W) were used as the illumination source, and also a data acquisition and processing system were used (Figure 1). To maintain the uniform light and reduce environmental noise, the system was covered by a case and the distance of the camera to the screen on which the samples were placed was adjusted manually (using a conveyor on which the camera was installed).

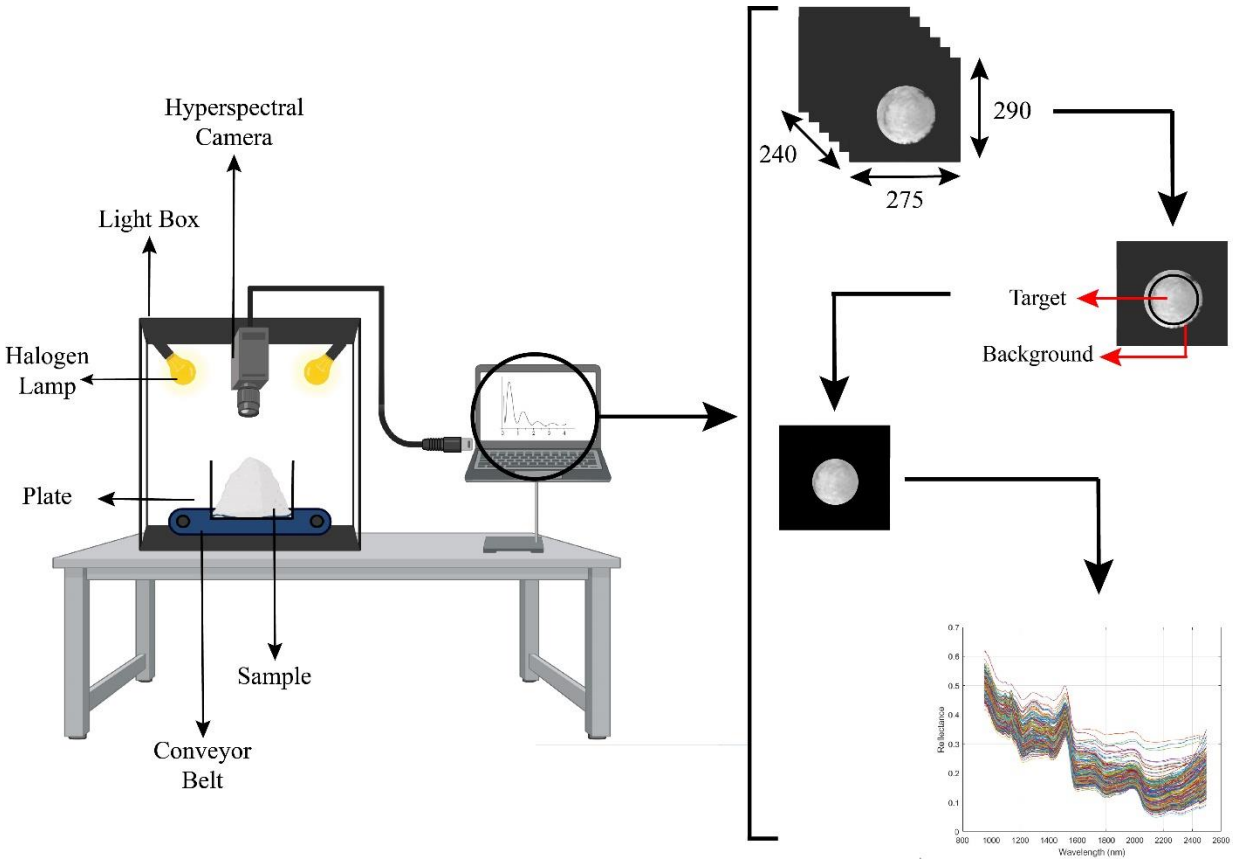

Figure 1. Image acquisition system alongside ROI selection and feature extraction processes.

The flour was placed on a circular plate with dimension and depth of 70 and 50mm, respectively and the flour surface was flattened using a thick paper stick without compression. Then was placed on a black, non-reflective 50 × 25 cm sample tray and To obtain clear and distortion-free hyperspectral images of samples, the intensity of the halogen light source, light source positioned from the horizontal plane, the sample away from the camera, exposure time, image acquisition speed were adjusted for 75% of total power, 55°, 52 cm, 9ms, 0.95 $cm.s^{-1}$, respectively. All of the 24 flours were placed on the tray without compression. The image hypercubes were composed of 367 × 368 × 169 pixels collected at 9.527 nm intervals between 950.105 and 2498.125 nm. The imaging system settings were optimised to ensure that the samples had the correct aspect ratio and to eliminate scanning bed vibrations induced by the manual adjustments.

2.2.2. Calibration procedure

Potential errors could include uneven illumination due to variations in the halogen lamp output, stray light reflections from surrounding surfaces, detector noise caused by environmental temperature fluctuations, or geometric distortions from misaligned components (Ma et al., 2023; Peng et al., 2024; Sun et al., 2024) . For calibration dark current correction was considered to address sensor noise by removing signals captured. Furthermore, white reference

calibration was applied for accurate normalization of reflectance values by accounting for variations in light intensity and sensor sensitivity, and finally wavelength calibration was utilized to minimize errors in spectral alignment by correcting shifts in wavelength detection. The images should be corrected for spectral and spatial radiation discrepancies induced by spectral response and grating scattering, dark current, and uneven light source intensity (He et al., 2023; Jiang et al., 2024). Therefore, black and white correction calculations were performed on the original hyperspectral image. The signal strength was reflected in the acquired raw image data. The spectral reflectance must be calculated by correcting for black and white. Black calibration with white calibration plate to set maximum emissivity (~99 %) and cover the dark correction lens cap to set the minimum reflectivity (~0 %) and then calibration image was calculated using Eq.1

$$I = \frac{I_0 - I_d}{I_0 - I_w} \quad (1)$$

Where I_0, I_d, and I_w are original hyperspectral image, blackboard calibrated image and whiteboard calibrated image, respectively.

2.2.3. Region of Interest (ROI) selection

The spectral image was extracted from the HSI Analyzer software (ITT Visual Information Solutions, Boulder, CO, USA). In each sample, the mass of CBF was placed in the center of the image. Based on the typical shape of the mass of CBF and the distribution of relevant spectral information within them, the sample can be separated from the background by simple threshold segmentation. Thus, a circular binary mask was applied for the selection of ROI in the hyperspectral images, assigning values 0 and 1 to the pixels corresponding to the background and CBF, respectively. Using the specified center and radius, this mask was applied to hyperspectral image to extract only the pixel data within the circle.

The spectral information within the ROI was concatenated to acquire the final spectral matrix. In this matrix, the rows and columns represented the number of CBF images and the wavelengths, respectively. In consequence, the 120 × 230 dimensional spectral matrix was obtained for chemical content prediction. The average spectrum of each image was then obtained by averaging the extracted spectral information from each pixel to create a representative spectrum for each CBF to establish the model (Figure 1). The ROI was consistently defined using a circular binary mask with a fixed center and radius, ensuring uniform application across all samples to minimize variability. Repeatability was verified by visually inspecting the extracted ROI on multiple samples, confirming that the method accurately isolated the CBF mass while excluding background pixels.

2.3. Qualification parameters

The chemical composition analysis was performed under dry weight basis using the Herrera et al. (2021) methods with some revisions. The revision was applied for measurement of carbohydrate component such as moisture and protein. Herra et al. (2021) for final glucose concentration used a GOD-PAP kit and a glucose standard solution (0−0.98 mg/dL).While in this research, to measure carbohydrates content (Eq. 2), the process involves measuring ash

by separating and analyzing the soluble and insoluble fiber fractions through gravimetric analysis after enzymatic treatment.

Carbohydrates (g/100 g) = 100 – [Ash (g/100 g) + Total Fat (g/100 g) + Moisture (g/100 g) + Protein (g/100 g)] (2)

Total dietary fiber was determined by the combination of enzymatic and gravimetric methods, using the Total Dietary Fiber Assay kit (kit K-TDFR, Megazyme, Ireland). For measurement of starch, the final glucose concentration was analyzed using a kit K-TSTA (Megazyme, Bray, Ireland), and a glucose standard solution (0-1 mg/dL) was used as control. The fat content was determined by extracting lipids using hexane and then gravimetric analysis was applied to quantify the extracted fat. In addition, nitrogen content through the Kjeldahl method was applied for the protein content.

2.4. Spectral image multivariate analysis

2.4.1. Set division

The research samples could ensure the performance of the model by being reasonably partitioned into the calibration set and prediction set. The samples in the calibration set should be representative and include the extreme value. In this research, Kennard-Stone (KS) and SPXY (sample set partitioning based on joint X-Y distance) methods have been applied to divide sample set. In the SPXY based KS method, spectral and reference variables were considered, and the spatial distance of the samples was calculated. The advantage of SPXY was that the partition sample set synchronously considered the spectral and concentration matrix, improving the capability of the model (Zhang et al., 2023). The distance between samples was calculated using Eq. 3-5.

$$d_x(p.q) = \sqrt{(x_p - x_q)^2} = \left|x_p - x_q\right|; p.q \in [1.n] \quad (3)$$

$$d_x(p.q) = \sqrt{(x_p - x_q)^2} = \left|x_p - x_q\right|; p.q \in [1.n] \quad (4)$$

$$d_{x.y}(p.q) = \frac{d_x(p.q)}{max_{p.q\in(1.n)}d_x(p.q)} + \frac{d_y(p.q)}{max_{p.q\in(1.n)}d_x(p.q)}; p.q \in [1.n] \quad (5)$$

After division using the KS method, dependence on data other than those concerned with the spatial distribution of the samples in the predictor space, X, it was set in such a way that a maximum distance between selected samples would obtain a uniform coverage (Karaziack et al., 2024). Ignoring response variables might have some subsets that are not representative in the relationship presented by predictors to responses as it was meant to be, hence resulting in this suboptimal model calibration. BY contrast, SPXY overcame these by incorporating X-Space-distance and Y-Space during the selection of samples. Luo et al. (2024) and Zhong et al. (2025) reported that , it has been further expounded that with SPXY factoring the variability jointly in both predictors and responses, the subset portrays the underlying relationship that does occur between X and Y-thus, more representative sets of calibration and validation which result in the enhancement seen in predictive modeling over spectral images. Finally, the SPXY method was chosen for set division.

205

206 2.4.2. Spectral pre-processing

207 Spectral data contains irrelevant information and noise, such as background noise, electrical noise, baseline
208 drift, and radio scattering, along with the chemical information contained in samples. Prior to modeling, spectral data
209 were preprocessed using traditional spectral preprocessing techniques such as standard normal variate (SNV),
210 probabilistic quotient normalisation (PQN), orthogonal signal correction (OSC), and mean centering (MC) to mitigate
211 the effects of these irrelevant elements and increase model accuracy (Erkinbaev et al., 2019). Further, some of the
212 advanced spectral preprocessing techniques like the external parameter orthogonalization (EPO) filter and generalised
213 least squares (GLS) weighting were used to see the effects of these advanced spectral preprocessing techniques on the
214 predictive accuracy of the models.

215 The EPO operates in a manner that is almost identical to that of OSC, but there are some differences. The
216 OSC function operates by orthogonalizing a response vector (y) or matrix (Y) to the data matrix (X), which is not
217 possible with unsupervised methods. EPO estimates the data's noise subspace without regard to Y orthogonality. As
218 a result, it can be used as a preprocessing step prior to applying unsupervised techniques (Saha et al., 2023). The GLS
219 method is capable of filtering out irrelevant information. This information is derived from the differences between
220 similar samples and then filtered from the original data matrix (Kucha et al., 2021).

221 2.4.3. Feature extraction

222 The spectral signal is highly complex and contains numerous parameters, necessitating the need for feature
223 extraction. The objective of feature extraction is to reduce dimensionality, computational complexity, and enhance
224 precision. In the context of spectral analysis applications, feature extraction is vital in identifying abnormalities in
225 spectra, distinguishing between various samples, and extracting useful features for modeling (Chen et al., 2024; Peng
226 et al., 2024). Despite the dissimilarity in their attributes and objectives, they all aim to portray the sample's nature via
227 spectroscopy. To predict the chemical content of CBF, four distinct feature extraction methods namely physiological
228 experiments identifying spectral profile changes (PHY), Competitive Adaptive Reweighted Sampling (CARS);
229 Continuous Wavelet Transform (CWT), and Iteratively Retaining Informative Variables (IRIV) have been employed.

230 The accurate detection of chemical bonds and any changes occurring in a component of the substance will
231 also be reflected through hyperspectral analysis. Consequently, when variations in carbohydrates, starch, protein and
232 fat occur in beans powder, a change in the hyperspectral image of the CBF is expected. This change is directly
233 associated with the variation in chemical properties. The central idea of the PHY method is to select features by
234 comparing two types of hyperspectral spectral lines in the CBF. This method focuses on extracting key features from
235 the spectral profiles, which are typically changes in frequency, amplitude, or phase, to understand the underlying
236 physiological processes. By isolating these spectral features, the PHY method aids in the prediction of physiological
237 states (Chen et al., 2024).

The CARS technique has been used for the selection of important wavelengths. CARS selects the critical wavelengths in a series of steps. The CARS technique uses exponentially decreasing function (EDF) and adaptive reweighted sampling (ARS) techniques, so the trivial weight of the wavelengths is eliminated (Luo et al., 2024). In this study, the feature wavelengths were evaluated using ten-fold cross validation. Several subsets of wavelengths are obtained after the execution of the loops. Finally, the effective wavelengths are defined as those subsets of wavelengths with the lowest root mean squared error of cross validation and the prediction models were built using the chosen wavelengths.

The CWT technique significantly enhances feature extraction accuracy in hyperspectral data by effectively capturing both local and global features. By effectively capturing spectral and spatial features, CWT facilitates improved data representation, leading to better model performance. CWT can streamline the feature extraction process, making it computationally feasible to handle large hyperspectral datasets while maintaining high accuracy (Sun et al., 2024).

The IRIV method was developed on the concept of a binary matrix shuffling filter (BMSF) for selecting variables. This approach uses model population analysis (MPA) to categorise all variables as highly informative, moderately informative, uninformative, and interfering (Saha et al., 2023). Through an iterative process, the interfering and uninformative variables are eliminated. The variables remaining after backward elimination are then selected as feature variables. In this investigation, a ten-fold cross validation with a maximum of ten principal components was conducted and specified wavelengths were utilised to develop the prediction models.

2.5. Machine learning and performance evaluation

2.5.1. Partial-least squares regression (PLSR)

PLSR, which is a highly effective and meaningful technique for data analysis, plays a critical role in analyzing spectral data considering its high performance. It can efficiently handle large, multicollinear datasets, and extract relevant information for predictions and interpretations. PLSR is adopted to search for potential linear combinations of wavelength variable (X) and chemical content (Y):

$$Y = X \times B + E \quad (6)$$

where B and E are the regression coefficient matrix and the regression residual matrix, respectively. The linear combinations, called latent variables (LVs), offer as much crucial, useful information as possible (Luo et al., 2024). The optimal quantity of LVs was determined when finally reaching the minimum RMSECV.

2.5.2. Support vector machine regression (SVMR)

PLSR assumes a linear spectrum–property relationship, which is not necessarily always true. Hence, a non-linear model like SVMR was employed as a comparison. SVMR is a non-parametric algorithm that maps the data into a higher feature space dimension and creates a discrete hyperplane using the kernel function. The kernel function minimizes the model complexity and maximizes the prediction accuracy. Different kernel functions have been used

in the developed nonlinear SVMR models to predict the chemical components of various products using HSI (Yin et al., 2023; Peng et al., 2024, Luo et al., 2024). In this study, four kernel functions consisting of the Radial basis function (RBF, Eq. 7), Polynomial (Eq. 8), Gaussian (Eq. 9), and Pearson universal (Eq. 10) were employed due to their computational efficiency.

$$f(xy) = e^{-\alpha\|x-y\|^2} \quad (7)$$

$$f(xy) = \frac{[(xy+1)^n]}{\sqrt{(xy+1)^n(y^2+1)^n}} \quad (8)$$

$$f(xy) = exp\left(-\frac{\|x_i-x\|^2}{2\sigma^2}\right) \quad (9)$$

$$f(xy) = \frac{1}{\left[1+(2\sqrt{\|x-y\|^2\sqrt{2^{\frac{1}{\beta}}-1)^2}}\right]^{\beta}} \quad (10)$$

where α, x, y, n, σ, and β are kernel dimension, feature vectors, polynomial degree, Gaussian and Pearson width, respectively. To optimize the Polynomial and Gaussian functions, the penalty factor (C) should be regularized. This parameter controls the SVMR performance by estimating the accuracy of the trained data point (Lin et al., 2023). Furthermore, the tuning parameter (γ) affects the mapping data into the higher dimensional space by controlling the width of the RBF and Pearson kernel (Zhang et al., 2023). Therefore, five levels of C (0.01, 0.1, 1, 10, and 100) and three levels of γ (0.01, 0.1, and 1) were applied to define the position of the hyperplanes. Subsequently, the performance of the developed model was assessed until it reached the best performance.

2.5.3. Temporal convolutional network-attention mechanism

Temporal Convolutional networks are a typical neural network model that integrates dilated and causal convolutions and the residual module. Temporal Convolutional Networks have been used for prediction tasks by modeling sequential data, allowing for the capturing of temporal dependencies with their dilated causal convolutions and extensive receptive fields (Qi et al., 2023; Luo et al., 2023; Wang et al., 2024). In this method, the convolution operation is calculated by Eq. 11.

$$F(p) = (xf_d)(p) = \sum_{i=0}^{k-1} f(i)x_{p-di} \quad (11)$$

Where *k, d, p-di* represent the size of the convolution kernel, expansion coefficient, and corresponding sequence in the convolution kernel. To enhance the temporal convolutional network prediction accuracy by selectively focusing on the most relevant time steps or features within the input sequence, the temporal convolutional network-attention mechanism (TCNA) method was applied. This allows the model to dynamically weigh important information, improving its ability to capture long-range dependencies and complex temporal patterns (Shuai et al., 2024). By assigning weight values to each variable, the attention mechanism focuses on important variables to improve the prediction result (Wang et al., 2024). The detailed calculation of the output attention vector can be found by Eq. 12 and 13.

$$G_i^d = \frac{\exp(g_i)}{\sum_{k=1}^{m} \exp(g_k)} \quad (12)$$

$$\beta_j = \frac{\exp\left(g_j^d\right)}{\sum_{k=1}^{n} \exp(g_k^d)} \quad (13)$$

where the [$g1$, …, gm], βj, n are block vector of the output vector, the output vector length, and the weight coefficient. In the model training process, the nodeNums was set to 38, the loss function was the mean absolute error , the optimizer was "adam", the batchSize was 38, and the number of epochs was 200.

2.6. Performance evaluation

In model analysis, all the CBF samples were divided into calibration, validation and prediction sets. The calibration set was used to adjust the model and conduct 10-fold cross-validation for obtaining all optimized model hyperparameters. To objectively evaluate the performance of the ML models (PLSR, SVMR, and TCNA) in predicting the content of carbohydrates, consistent model parameters were adopted for all models in the corresponding type of output. All the model analysis was carried out using the Matlab 2023 software and prediction performance of the model was mainly evaluated in terms of the coefficient of determination (R2), root mean squared error (RMSE), and relative percentage deviation (RPD). The calculation of the evaluation indicators and the evaluation criteria for model performance were described in the literature (He et al., 2023; Qi et al., 2023; Luo et al., 2024; Peng et al., 2024).

3. Results and discussion

3.1. Chemical analysis

The chemical composition of various CBF were presented in Table1. The average value of protein of all the treated samples was more than in the control samples. However, the difference of all samples was not significant. The average value of protein in treated samples, 4.98 g/100 g was more than the control CBF. Similarly, the average value of fat, starch and carbohydrate of treated samples were more than the controls CBF, even though significant difference was not observed between most cases. The amount of fat, starch and carbohydrate of control samples were 0.72 g/100 g, 38.16 g/100 g and 66.95 g/100 g, while for the treated CBF were 1.03 g/100 g, 41.50 g/100 g and 70.04 g/100 g, respectively.

It seems hydration-dehydration treatment did not considerably increase the absolute amount of protein in CBF. Instead, it improves the quality and bioavailability of the protein. After the treatment, the removal of water results in a concentration of all solid components, including fat and starch. Thus, the relative percentage of fat and starch in the bean's dry weight might appear slightly increased, but this is due to the concentration effect rather than an actual increase in fat content (Wainaina et al., 2021; Alfaro-Diaz et al., 2023). Also, Table 1 shows the correlation coefficient values of the quantitative regression for all CBF were above 0.980, indicating an acceptable linear quantitative relationship. Even though the differences were not significant, the observed variations in protein, fat, starch, and carbohydrate content between treated and control samples can be attributed to changes induced by the hydration-dehydration treatment at a molecular level. The treatment could cause structural changes to proteins such

as unfolding or denaturation, which might enhance their solubility and bioavailability without affecting the overall quantity significantly. Similarly, the concentration effect resultant of water removal could accordingly enhance the relative proportions where such solid components like fat and starch became more pronounced due as a result of an intensive dry matter content. Hydration-dehydrations may change the manner of arrangement of starch granulature, improving digestability, and accessibility of hydrogenous nutrients. Such mentioned above molecular interactions demonstrate also how the treatment could really influence the quality rather or even more than the type, of the absolute absolute composition of the bean flour basic constituents (Alfaro-Diaz et al., 2023; Bai et al., 2024).

Table 1. Chemical content of untreated and treated beans powder and correlation coefficient values of the quantitative regression for all powder content

No. Sample	Qualification parameter									
	Control					Treated				
	Protein (g/100 g)	Fat(g/100 g)	Starch(g/100 g)	Carbohydrate(g/100 g)	R^2	Protein(g/100 g)	Fat(g/100 g)	Starch(g/100 g)	Carbohydrate(g/100 g)	R^2
1	16.14±1.23^{a}	0.56±0.08^{b}	36.21±3.48^{e}	65.38±5.45^{g}	0.992	18.72±2.04^{a}	0.68±0.09^{c}	37.30±3.01^{e}	68.47±6.21^{g}	0.983
2	17.13±1.35^{a}	0.67±0.09^{bc}	37.41±4.36^{e}	66.45±4.98^{g}	0.995	20.07±1.82^{a}	1.01±0.12^{d}	40.32±4.28^{e}	69.7±8.66^{g}	0.989
3	16.71±1.51^{a}	0.62±0.07^{b}	37.18±5.72^{e}	65.45±4.82^{g}	0.984	19.43±1.56^{a}	0.94±0.06^{d}	40.28±6.34^{ef}	69.17±7.62^{g}	0.981
4	17.78±1.68^{a}	0.78±0.06^{bc}	38.98±7.24^{e}	67.46±6.13^{g}	0.990	21.01±1.75^{a}	1.09±0.9^{d}	47.51±7.39^{f}	70.45±5.82^{g}	0.984
5	17.10±1.52^{a}	0.67±0.09^{b}	37.30±9.34^{e}	66.43±5.88^{g}	0.982	20.00±1.91^{a}	0.99±0.05^{d}	40.72±9.64^{ef}	69.53±8.26^{g}	0.980
6	17.65±2.26^{a}	0.74±0.08^{b}	37.94±5.36^{e}	67.30±8.41^{g}	0.988	20.68±2.34^{a}	1.04±0.92^{d}	41.39±6.33^{e}	70.07±10.27^{g}	0.981
7	18.40±2.55^{a}	0.84±0.13^{bc}	38.74±4.78^{e}	67.86±9.22^{g}	0.995	21.54±3.75^{a}	1.15±0.12^{d}	41.89±5.36^{ef}	70.90±8.22^{g}	0.992
8	18.66±3.37^{a}	0.87±0.09^{c}	39.03±6.34^{e}	68.12±10.07^{g}	0.993	21.80±2.36^{a}	1.22±0.11^{d}	42.56±7.25^{e}	71.14±6.99^{g}	0.988
9	16.57±2.88^{a}	0.60±0.08^{b}	36.98±5.39^{e}	65.65±8.24^{g}	0.986	19.32±1.78^{a}	0.93±0.08^{cd}	40.08±9.37^{ef}	69.12±8.34^{g}	0.985
10	18.03±3.07^{a}	0.87±0.09^{c}	38.53±4.27^{e}	67.64±9.36^{g}	0.993	21.18±1.82^{a}	1.11±0.15^{d}	41.72±6.37^{ef}	70.59±7.22^{g}	0.990
11	18.83±2.55^{a}	0.89±0.09^{c}	39.40±6.23^{e}	68.57±8.24^{g}	0.995	21.93±1.55^{a}	1.22±0.13^{d}	43.05±8.25^{ef}	71.47±9.47^{g}	0.988
12	17.65±3.01^{a}	0.60±0.05^{b}	40.28±7.50^{e}	67.63±8.81^{g}	0.989	20.61±1.72^{a}	1.03±0.11^{d}	41.19±9.47^{ef}	69.94±8.22^{g}	0.985

240 samples (24samples × 10 replicates) of common beans powder. Mean ± sd: mean content with standard deviation. The lowercase letters (a, b, c, etc.) indicate a significant difference at a level of $P < 0.05$.

3.2. Spectral characteristics

346 The spectral lines have been changed according to applied pre-processing methods (Figure 1). The spectral
347 lines of MC, PQN and GLS become diffusers, while the dispersion of OSC and SNV looks similar to the original
348 spectra. However, a particular preprocessing method cannot be selected only from the variation of spectral line
349 dispersion, because no algorithm is the most suitable and finding the best method to achieve the research goal usually
350 requires iterations (Aulia et al., 2022; Chen et al., 2024).

351 Figure 2.a shows the raw average curves of the spectra reflectance (890–2500 nm) obtained from 240 CBF
352 samples with different chemical contents. In the wavelength range the waveforms revealed a similar spectral trend for
353 different CBF. Nevertheless, the trend of some spectrum curves was irregular, which could be attributed to the
354 excessive energy at the scanning step and the decreased noise reduction effect (Zhang et al., 2023). Figure2.b illustrates
355 the range of average hyperspectral wavelength (without any preprocessing) and the spectral reflectivity was 0.12–0.5,
356 which were selected for the subsequent work. The identified spectral regions corresponding to various chemical bonds
357 and functional groups provide valuable information on the chemical composition and quality of CBF. The peaks
358 around 1085 and 1142 nm was related to fat and starch, respectively, which were very important in understanding
359 carbohydrate and lipid contents that directly affect the energy value and texture of the flour. Reflectance around 1235
360 nm could be associated with starch, but differences were observed in this zone for the CBF, suggesting the presence
361 of carbohydrates linked with fat and starch (Yu et al., 2022). In fact, fat and starch are one of the main constituents in
362 CBF, and responsible for many of the aforementioned reflectance peaks with 1257–1285 and 1361–1389 nm
363 (Hernández-Hernández et al., 2022).

364 The spectral features for the region between 1420 and 1520 nm could also be ascribed to N–H stretching,
365 which normally refers to the presence of protein, the nutritional value component, or functional properties essential
366 for holding moisture and promoting dough-forming capability (Kaur et al., 2024). On one hand, its region around
367 1600–1700 nm encompasses only the two Amide regions, the A and B bands in particular. This region pays special
368 emphasis to the structural and contents preoccupation of protein due to the interaction between itself and the
369 carbohydrate components or the already formed protein-carbohydrate complexes affecting viscosity, water retentions,
370 and texturing during processing. The region between 1650 and 1710 nm is allocated to the first sign of C-H stretching.
371 In the 1800–1870 nm region, combination bands involving N-H stretching and bending vibrations are prominent,
372 indicating the presence of amide bonds in carbohydrate (Hernández-Hernández et al., 2022). In addition, the broad
373 peaks between 1900 and 1980 nm were related to the complexity of carbohydrate mixtures, reflecting variability in
374 starch and fiber content, with implications for flour digestibility, texture, and cooking properties. A relatively broader
375 region between 1900 and 1980 nm region, while specific to carbohydrate, shows bands related to C-H, N-H, and O-H
376 groups, reflecting a mixture of these functional groups in the CBF. The spectra display broad peaks and overlapping
377 signals, indicating complex mixtures of carbohydrates or amino acids with varied reflectance suggesting differences
378 in concentration or composition. Prominent peaks found in the spectra around ~1520 nm and ~1980 nm, align with
379 regions associated with carbohydrate reflectance, and broader peaks around 2320 and 2430 nm correspond to
380 combination bands involving various functional groups (Yu et al., 2022; Kaur et al., 2024; Sim et al., 2024).

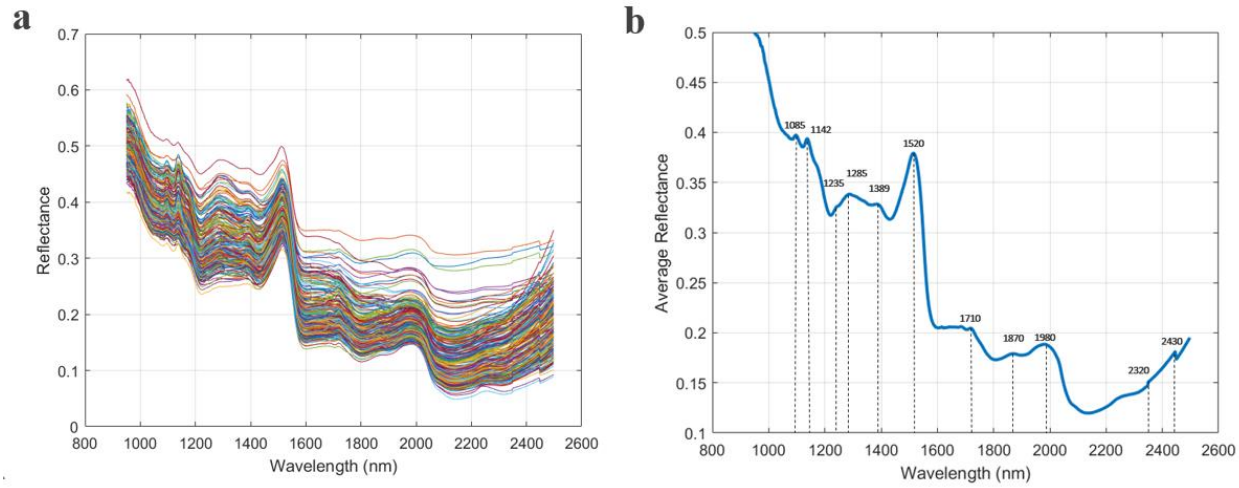

Figure 2. a) Raw acquired spectra, b) Average reflectance spectra of CBF samples

3.3. Model evaluation

3.3.1. Content regression models

The spectra and the corresponding carbohydrate values in the calibration set were used as the input of the model, and the whole pre-processing methods and ML model were trained in a supervised way (Table 2). The samples in the validation set were used to test the model performance and tune the model parameters, while the samples in the prediction set were used to evaluate the performance of the applied models. Although the PLSR method provided good results in the research by Hernández-Hernández et al. (2022) and Luo et al. (2024) to predict the chemical properties of food products, in this research, the PLSR model did not achieve a high accuracy. The R2 and RMSE of PLSR were 0.716 and 0.456, respectively. By applying the SNV pre-processing method, the prediction accuracy increased (R2= 0.752, RMSE= 0.401), even though the OSC method had a negative effect. Similarly, Qi et al. (2023), Yin et al. (2023) had reported the effect of SNV preprocessing method in PLSR models and revealed that SNV could significantly decrease the error of prediction. The SNV helped to reduce the noise in the data by focusing on the mean-centered data and standardizing it, which could help mitigate the effects of random noise (Qi et al., 2023; Yin et al., 2023; Saha et al., 2023).

SVMR with different kernel functions, penalty factor and tuning parameters were analyzed and the best kernel and variable were selected as the optimized SVMR for modeling (Table 1s). Based on the results, SVMR with RBF kernel, 10 level of C and 0.1 level of γ was considered for carbohydrate prediction by applying pre-processing (R2 = 0.893, RMSE = 0.366). Although Polynomial, Gaussian, and Pearson kernels could model non-linear relationships they require careful tuning of the tuning degrees and are prone to overfitting if the degree is too high. The RBF kernel, by contrast, offers a good balance between complexity and generalization which was demonstrated by Luo et al. (2023) and Sun et al. (2024). Contrary to the application of OSC in PLSR model, this pre-processing technique significantly increased the accuracy of the SVMR model (R2= 0.902, RMSE= 0.351) and PQN and MC

methods decreased the accuracy of the model. Also, SNV method increased the accuracy of the model, but the best result was obtained by OSC. In similar way, Saha et al. (2023) and Zhang et al. (2023) Applied various preprocessing methods such as OSC for predicted of protein content in single chickpea seed and reported that the accuracy of OSC was acceptable. OSC had ability to specifically remove variations that are orthogonal to the response variable, thereby enhancing the relevance of the data to the prediction task, improving model interpretability, reducing multicollinearity, and improving model performance (Saha et al., 2023; Zhang et al., 2023).

The TCNA method without any pre-processing presented a good amount of R2 (0.956), RMSE (0.21) and RPD (2.05). Interestingly, some preprocessing methods reduced the level of performance parameters. In fact, TCNA uses both convolutions and attention mechanisms to learn relevant features in time-series data. It seems PQN, MC, EPO and GLS adjusted the data based on distribution assumptions, which might lead to the model losing access to raw patterns and loss of important temporal dependencies (Barbedo, 2023). SNV (R2: 0.956, RMSE: 0.219, RPD: 2.857) and OSC (R2: 0.957, RMSE: 0.203, RPD: 2.903) methods increased prediction accuracy almost equally and with a slight difference compared to the N-TCNA. However, N-TCNA spent less time on analysis and in general, the analysis time and accuracy of PLSR<SVMR<TCNA. Wang et al. (2024) compared the accuracy and time analysis of multi-layer perceptron (MLP) and TCNA for prediction of diverse rare ginsenoside contents in *Panax ginseng* through hyperspectral imaging. They revealed although the prediction performance of TCNA was better than MLP, the difference of their time interfence was significant. Similarly, Qi et al. (2023) applied MLP, SVM, PLS and TCN to determine soluble solid content of crown pears and they reported the accuracy of MLP < PLS < SVM <TCN. TCNA exceled at learning complex non-linear relationships in data through multiple layers of transformations. While PLSR and SVMR were powerful methods to predict the quality parameters, they could struggle with highly complex non-linearities, especially in high-dimensional time-series data (Barbedo, 2023; Qi et al., 2023; Wang et al. (2024).

Table 2. Prediction results of carbohydrate content in CBF using full spectrum and ML methods with different pre-processing techniques.

Model	Pre processing	Calibration set		Validation set		Prediction set			Time (m)
		R_c^2	$RMSE_c$	R_v^2	$RMSE_v$	R_p^2	$RMSE_p$	RPD_p	
PLSR	N	0.795	0.371	0.755	0.391	0.716	0.456	1.963	0.093
	MC	0.797	0.37	0.767	0.39	0.727	0.451	2.05	0.095
	PQN	0.798	0.366	0.778	0.387	0.729	0.436	2.267	0.099
	SNV	0.785	0.344	0.782	0.38	0.752	0.401	2.903	0.095
	OSC	0.794	0.375	0.754	0.395	0.715	0.464	1.982	0.094
	EPO	0.799	0.357	0.779	0.381	0.746	0.405	2.857	0.096
	GLS	0.798	0.362	0.779	0.385	0.735	0.411	2.468	0.095
SVMR	N	0.924	0.289	0.908	0.326	0.893	0.366	3.655	0.152

	MC	0.919	0.302	0.904	0.334	0.865	0.382	3.455	0.152
	PQN	0.92	0.301	0.907	0.332	0.891	0.373	3.561	0.175
	SNV	0.955	0.231	0.916	0.317	0.899	0.352	3.739	0.163
	OSC	0.958	0.202	0.917	0.316	0.902	0.351	3.859	0.168
	EPO	0.925	0.285	0.912	0.325	0.896	0.363	3.889	0.172
	GLS	0.928	0.281	0.913	0.32	0.898	0.36	3.852	0.158
TCNA	N	0.99	0.085	0.974	0.155	0.956	0.21	4.685	0.155
	MC	0.982	0.136	0.965	0.172	0.949	0.24	4.116	0.156
	PQN	0.979	0.15	0.962	0.184	0.945	0.252	3.963	0.159
	SNV	0.989	0.105	0.974	0.155	0.957	0.219	4.682	0.161
	OSC	0.991	0.082	0.975	0.151	0.957	0.203	4.695	0.156
	EPO	0.984	0.135	0.971	0.165	0.953	0.233	4.155	0.155
	GLS	0.985	0.126	0.972	0.163	0.954	0.221	4.236	0.154

3.3.2. Model development with feature wavelength

The optimized pre-processing methods were chosen for feature extraction and development of PLSR, SVMR and TCNA models. Although the PHY, IRIV and CWT affected the performance indexes of PLSR, the accuracy prediction of SNV-CARS- PLSR was increased significantly (R2p: 0.931, RMSEp: 0.237, RPDp: 3.653) (Figure 3). The positive effectiveness of CARS method on the PLSR models were claimed by Saha et al. (2023), Zhang et al. (2023), and Li et al. (2024). They reported the CARS method improves the accuracy of PLSR by selecting the most informative and relevant variables, reducing noise and overfitting, and ensuring the model focuses on the strongest signals in the data. In addition, CARS selects variables that are less redundant, improving latent factors and selects variables based on their contribution to the PLSR model.

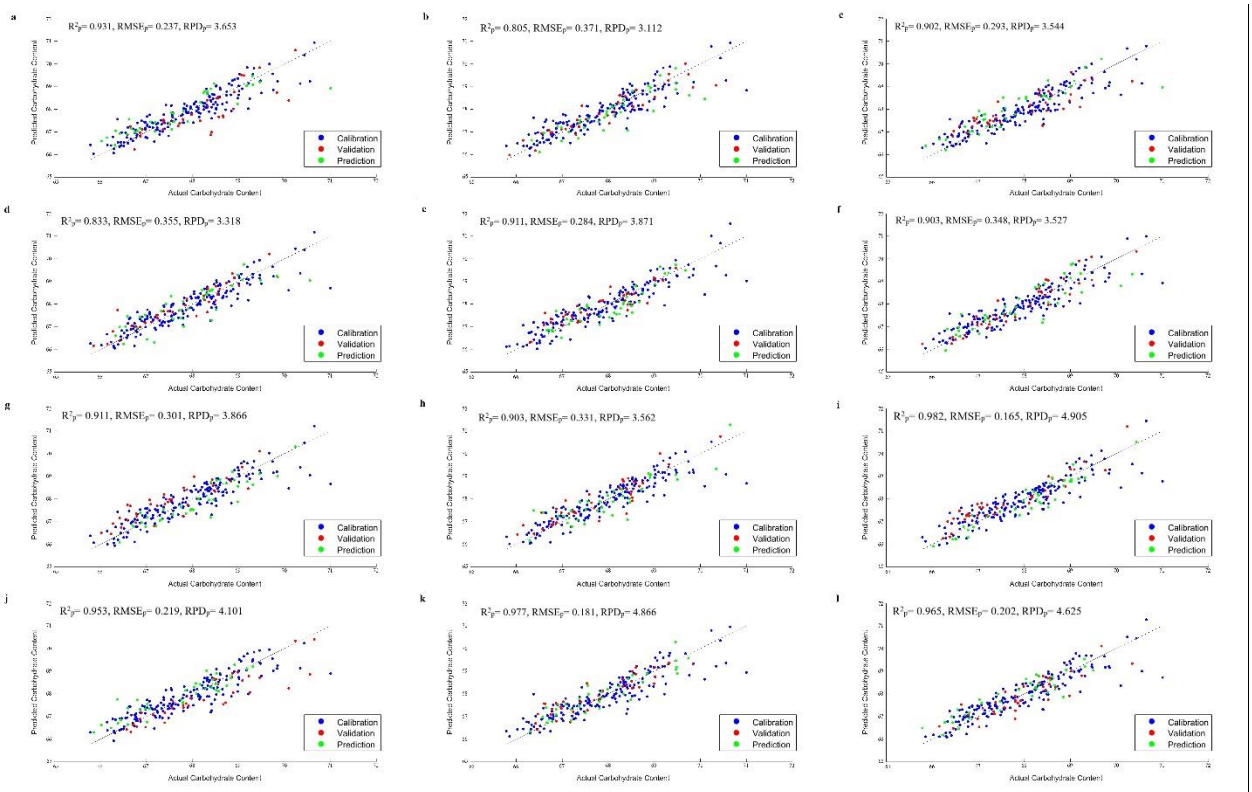

Figure 3. The regression curve for the content prediction of CBF based on the effective wavelengths with topology of; (a) EPO-CARS-PLSR, (b) EPO-CWT-PLSR, (c) EPO-IRIV-PLSR, (d) EPO-PHY-PLSR, (e) OSC-CARS-SVMR, (f) OSC-CWT-SVMR, (g), OSC-IRIV-SVMR, (h) OSC-PHY-SVMR, (i) OSC-CARS-TCNA, (j) OSC-CWT- TCNA, (k) OSC-IRIV-TCNA, (l) OSC-PHY-TCNA

The performance of OSC-CWT was poor in the SVMR model compared to the other feature wavelengths (R2p: 0.903, RMSEp:0.348, RPDp: 2.511) and similar to PLSR model, the CARS method improved the prediction accuracy of carbohydrate content in CBP. However, the level of R2p, RMSEp and RPDp of the developed SVMR model was less than PLSR. Saha et al. (2023) and Leo et al. (2024) used CARS and IRIV of feature wavelengths for rapid protein and soluble solid content prediction of chickpea and mandarin, respectively. They applied PLSR and SVMR model and before developing the ML model, the error of PLSR was greater than SVMR. Conversely, the CARS and IRIV enhanced the R2 and RMSE of PLSR by which the accuracy of this method took over the SVMR. Perhaps incompatibility between feature selection and SVMR kernel occurred (Saha et al., 2023). Furthermore, both CARS and IRIV methods aim to reduce the feature space by selecting only the most important variables. While this can reduce overfitting and simplify the model, it can also lead to over-simplification. SVMR works well with complex datasets, and removing too many variables can result in loss of useful information, particularly in nonlinear relationships. This loss of information might degrade the ability of SVMR to find optimal hyperplanes or decision boundaries in the feature space (Yin et al., 2023; Leo et al., 2024).

Similar to the PLSR and SVMR, the CARS method presented the best model for the TCNA with R2p: 0.982, RMSEp: 0.165 and RPDp : 4.905. Similarly, SVMR model, the most poor topology was OSC-CWT- TCNA (R2p: 0.953, RMSEp: 0.219 and RPDp: 4.101). Overall, the level of performance parameters after development was SVMR<PLSR<TCNA. Comparative research among the algorithms for performance comparison of PLSR, SVMR, and TCNA presneted interesting strengths and limits in data handling and modeling of complex relationships. The highest prediction ability in carbohydrate content of PLSR was particularly achieved along with the use of a variable selection technique, especially CARS and IRIV, which showed outstanding capabilities in filtering and extracting information about latent variables to summarize the input effectively. While the SVMR in general did well in capturing nonlinear relationships due to kernel-based methods, their performance was affected adversely in the case of the SVMR. This could be because probably some of the selected feature selection methods are incompatible with them, and the over-shrinking of the feature space resulted in losing information that was crucial for its nonlinear captures (Qi et al., 2023). On the other hand, TCNA emerged the best compared to the PLSR and SVMR methods. This acts as a sign of suitability to handle such complex data that is characterized by high-dimensional feature spaces together with nonlinear relationships (Wang et al., 2024). It has thus given the best trade-off between accuracy and robustness for TCNA: R2p = 0.982, RMSEp = 0.165, RPDp = 4.905, while for the PLSR and SVMR with lower R2p values and higher RMSEp, they both showed limitations in modeling more complex relationships with reduced feature spaces or introducing nonlinearity. This comparison underlines the importance of matching the model choice with the data structure and the complexity of the relationships modeled.

The robustness of TCNA to predict the quality parameters of various products was demonstrated in the literature (Qi et al.,2023; Wang et al., 2024; Shuai et al., 2024). Qi et al. (2023) reported that MLP-CNN-TCN model obtained better prediction performance compared to the SVMR model, with a prediction determination coefficient of 0.956 for solid soluble content of pear. They reported TCNA excels at capturing temporal patterns and long-term dependencies, which SVMR struggles with and also TCNA scales better with large datasets compared to SVMR, which can struggle with high-dimensional data. Wang et al. (2024) compared the prediction accuracy of three deep learning models consist of MLP, TCN, and TCNA and reported the optimized TCNA presented minimum error. Overall, wavelength extraction methods can improve accuracy by eliminating irrelevant features but might reduce accuracy if non-linear interactions are removed (Shuai et al., 2024).

Observed differences across performances of PLSR, SVMR, and TCNA bear important effects from a practical point of view from actual applications in the CBF treatment industry. Among them, the strength provided by PLSR may perfectly suffice to tackle difficult multilinearity and linear relationships for routine quality control-type demands where the rapid and reliable computation of chemical components is mostly required as routine tasks with minimum computational cost involvement (Aulia et al., 2022). While this may be a limitation, the capability of SVMR to model nonlinear relationships provides an added advantage in applications where a complex dataset needs to be handled, for instance, property prediction influenced by intricate interactions of several variables, provided the feature selection is optimized carefully to avoid loss of information (Yin et al., 2023; Peng et al., 2024, Luo et al., 2024). TCNA may turn out much more precise and robust in such cases when high-dimensional datasets and complicated

relationships are involved. For some tasks requiring high accuracy-like formulation optimization or the design of products with special nutritional or functional features-TCNA could become of real value. Model selection depends on a particular task and should be done with regard to the desired accuracy, available computational resources, and data relationship complexity (Qi et al., 2023; Luo et al., 2023; Wang et al., 2024).

3.4. Visualization of carbohydrate distribution

Visual prediction maps portrayed concentration changes between samples and even inside one sample, which the naked eye and conventional industrial color cameras cannot do. Furthermore, the visualisation findings indicated that HSI has a significant advantage over traditional spectroscopy in chemical composition and spatial contaminant identification of various products (Aulia et al., 2022; Zhang et al., 2023). Figure 4 illustrates the best OSC-CARS-TCNA model to predict distribution of carbohydrate content. The image with the linear colour scale on the right intuitively showed the distribution of carbohydrate in CBF samples. Variations of the ingredients were allocated on a linear colour scale. The carbohydrate content in the CBF was obviously differentiated from the color, and the distribution was uneven. It is concluded the change of carbohydrate content in CBF would be distinguished through color changes, and the visualization detection of carbohydrate content in CBF was realized. Therefore, the visualization images from HSI could be easily used for the detection of carbohydrate. That was a simple and useful method used for a fast and accurate non-destructive visible system. As compared to single point detection technology, HSI technology could accomplish the visualization of carbohydrate content in any local area of CBF and contribute to the integrated assessment for the quality of CBF.

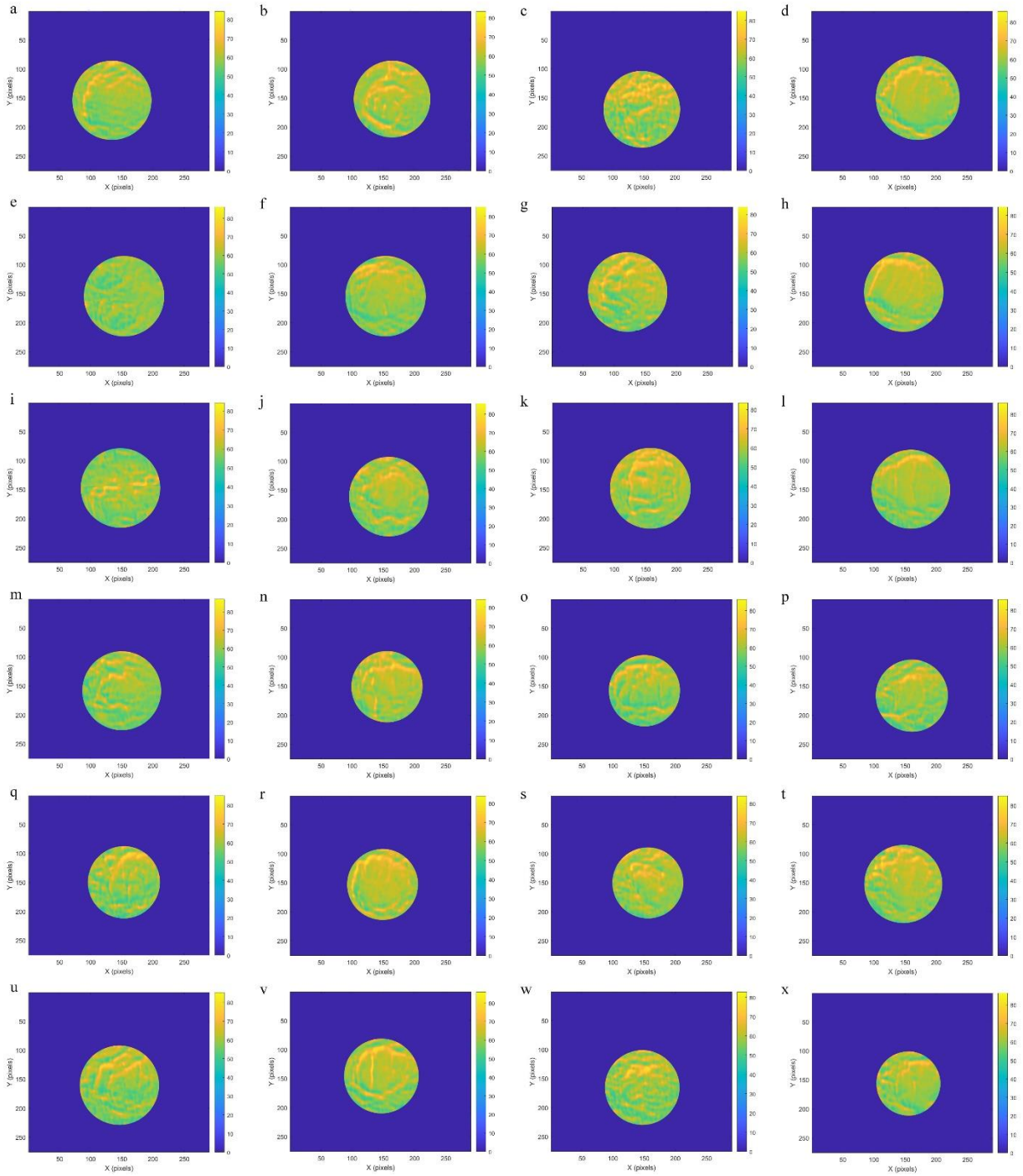

514

515

516

517

518

Figure 4. Visualization map of carbohydrate content in CBF. (a) IT-134 (b) IT-206 (c) IT-380 (d) IT-449 (e) IT-874 (f) SP-171 (g) SP-496 (h) GR-430 (i) GR-833 (j) AL-924 (k) AL-1237 (l) CR-1417 (m) IT-134 treated (n) IT-206 treated (o) IT-380 treated (p) IT-449 treated (q) IT-874 treated (r) SP-171 treated (s) SP-496 treated (t) GR-430 treated (u) GR-833 treated (v) AL-924 treated (w) AL-1237 treated (x) CR-1417 treated

4. **Conclusion**

In this work, we contribute to the use of HSI for quality detection of common bean's flour. A new quality detection model for CBF that combines HSI, ML, and physiological experiments was proposed. Our results support the feasibility of using ML algorithms for accurate quality detection of CBF to guide the establishment of future inspection methods. The hyperspectral of CBF was processed to convert the high-dimensional image data into a column vector with only a few spectral features. Image dimensionality reduction, spectral preprocessing, and spectral feature extraction methods were used to achieve this. Cross-modeling of each method was then performed to obtain a highly accurate model for quality detection and variety identification of CBF. The outputs demonstrated although deep learning presents more accuracy than ML models, the applied ML models not only provided acceptable and reliable accuracy but also affect significantly in time-analyzing. Therefore, the online and real-time systems can use ML models by considering optimization process. In addition, visualization output of the current research revealed that the developed models and system can integrate to some intelligent sensors for internet of things (IoT) and digitalization aims.

However, some limitations still need to be overcome in the future. First, the spectral and chemical content data can be further normalized and denoised to reduce the impact of individual differences. Meanwhile, various detection methods such as mass spectrometry imaging should be jointly applied to determine whether the distribution uniformity of prediction compounds and their characteristic structural differences affect the prediction accuracy and selection of effective wavelengths. Moreover, as portable HSI devices can better meet the market demand, it will be the primary task to develop convenient HSI devices based on the optimal ML model to achieve more effective and comprehensive quality evaluation of food materials in the future.

Funding

This work is supported by University of Basilicata and the project funded by Ministry of Science, Italy and is supported under funding number 296/2023-2597.

CRediT authorship contribution statement

Mahdi Rashvand: Conceptualization, Data curation, Methodology, Software, Writing—original draft; **Giuliana Paterna:** Data curation, Methodology , Writing—original draft; Sabina Laveglia: Data curation, Methodology; **Hongwei Zhang**: Writing—review and editing; **Alex Shenfield:** Writing—review and editing , **Tania Gioia:** Project administration, Supervision, Visualization; **Giuseppe Altieri:** Writing—review and editing , **Giovanni Carlo Di Renzo:** Writing—review and editing , **Francesco Genovese:** Conceptualization, Project administration, Supervision, Visualization,Validation, Writing—review and editing

Declaration of Competing Interest

The authors declare that they have no known competing financial interests or personal relationships that could have appeared to influence the work reported in this paper.

Data availability

Data will be made available on request.

References

Alfaro-Diaz, A., Escobedo, A., Luna-Vital, D. A., Castillo-Herrera, G., & Mojica, L. (2023). Common beans as a source of food ingredients: Techno-functional and biological potential. Comprehensive Reviews in Food Science and Food Safety, 22(4), 2910-2944. https://doi.org/10.1111/1541-4337.13166.

Aulia, R., Kim, Y., Amanah, H. Z., Andi, A. M. A., Kim, H., Kim, H., ... & Cho, B. K. (2022). Non-destructive prediction of protein contents of soybean seeds using near-infrared hyperspectral imaging. Infrared physics & technology, 127, 104365. https://doi.org/10.1016/j.infrared.2022.104365.

Bai, Q., Li, M., Zhou, J., Imran, A., de Souza, T. S., Barrow, C., ... & Suleria, H. A. (2024). Influence of processing methods on phytochemical composition of different varieties of beans (Phaseolus vulgaris). Food Reviews International, 40(7), 1941-1979. https://doi.org/10.1080/87559129.2023.2245026.

Barbedo, J. G. A. (2023). A review on the combination of deep learning techniques with proximal hyperspectral images in agriculture. Computers and Electronics in Agriculture, 210, 107920. https://doi.org/10.1016/j.compag.2023.107920.

Chen, B., Shi, B., Gong, J., Shi, G., Jin, H., Qin, T., ... & Wang, Z. (2024). Quality detection and variety classification of pecan seeds using hyperspectral imaging technology combined with machine learning. Journal of Food Composition and Analysis, 131, 106248. https://doi.org/10.1016/j.jfca.2024.106248.

Fdez-Vidal, X. R., Fernández-Canto, N., Romero-Rodríguez, M. Á., Ramos-Cabrer, A. M., Pereira-Lorenzo, S., & Lombardero-Fernández, M. (2024). Neural networks allow the automatic verification of the type of flour, analysing the starch granule morphology, to ensure the protected geographical indication 'Galician Bread'. Food Control, 158, 110198. https://doi.org/10.1016/j.jfca.2024.106425.

583 Food and Agriculture Organization of the United Nations. (2023). "FAOSTAT: Crops and livestock products."
584 Retrieved from FAO.

585 Guan, H., Zhang, Z. T., Bai, L., Chen, L., Yuan, D., Liu, W., ... & Yan, G. (2024). Multi-spectra combined with
586 Bayesian optimized machine learning algorithms for rapid and non-destructive detection of adulterated functional
587 food Panax notoginseng powder. Journal of Food Composition and Analysis, 106412.
588 https://doi.org/10.1016/j.jfca.2024.106412.

589 He, H. J., Chen, Y., Li, G., Wang, Y., Ou, X., & Guo, J. (2023). Hyperspectral imaging combined with chemometrics
590 for rapid detection of talcum powder adulterated in wheat flour. Food Control, 144, 109378.
591 https://doi.org/10.1016/j.foodcont.2022.109378.

592 Hernández-Hernández, C., Fernández-Cabanás, V. M., Rodríguez-Gutiérrez, G., Fernández-Prior, Á., & Morales-
593 Sillero, A. (2022). Rapid screening of unground cocoa beans based on their content of bioactive compounds by NIR
594 spectroscopy. Food Control, 131, 108347. https://doi.org/10.1016/j.foodcont.2021.108347.

595 Herrera, M. D., Reynoso-Camacho, R., Melero-Meraz, V., Guzmán-Maldonado, S. H., & Acosta-Gallegos, J. A.
596 (2021). Impact of soil moisture on common bean (Phaseolus vulgaris L.) phytochemicals. Journal of Food
597 Composition and Analysis, 99, 103883. https://doi.org/10.1016/j.jfca.2021.103883.

598 Jiang, X., Liu, Q., Yan, L., Cao, X., Chen, Y., Wei, Y., ... & Xing, H. (2024). Hyperspectral imaging combined with
599 spectral-imagery feature fusion convolutional neural network to discriminate different geographical origins of
600 wolfberries. Journal of Food Composition and Analysis, 132, 106259. https://doi.org/10.1016/j.jfca.2024.106259.

601 Karaziack, C. B., Vidal, C., Pasquini, C., Barbin, D. F., & Viotto, W. H. (2024). Application of near-infrared
602 hyperspectral imaging for determination of cheese chemical composition. Journal of Food Composition and Analysis,
603 127, 105994. https://doi.org/10.1016/j.jfca.2024.105994.

604 Kaur, S., Singh, N., Sharma, P., Ananthan, R., Singh, M., Singh, A. K., & Bhardwaj, R. (2024). Optimizing Protein
605 Content Prediction in Rice Bean (Vigna umbellata L.) by Integrating Near-Infrared Reflectance Spectroscopy, MPLS,
606 Deep Learning, and Key Wavelengths Selection Algorithms. Journal of Food Composition and Analysis, 106655.
607 https://doi.org/10.1016/j.jfca.2024.106655.

608 Kucha, C. T., Liu, L., Ngadi, M., & Gariépy, C. (2021). Assessment of intramuscular fat quality in pork using
609 hyperspectral imaging. Food Engineering Reviews, 13, 274-289. https://doi.org/10.1007/s12393-020-09246-9.

610 Li, D., Park, B., Kang, R., Chen, Q., & Ouyang, Q. (2024). Quantitative prediction and visualization of matcha color
611 physicochemical indicators using hyperspectral microscope imaging technology. Food Control, 163, 110531.
612 https://doi.org/10.1016/j.foodcont.2024.110531.

613 Lin, Y., Ma, J., Wang, Q., & Sun, D. W. (2023). Applications of machine learning techniques for enhancing
614 nondestructive food quality and safety detection. Critical Reviews in Food Science and Nutrition, 63(12), 1649-1669.
615 https://doi.org/10.1080/10408398.2022.2131725.

Liu, Q., Zhang, W., Zhang, B., Du, C., Wei, N., Liang, D., ... & Pan, L. (2022). Determination of total protein and wet gluten in wheat flour by Fourier transform infrared photoacoustic spectroscopy with multivariate analysis. Journal of Food Composition and Analysis, 106, 104349. https://doi.org/10.1016/j.jfca.2021.104349.

Luo, N., Xu, D., Xing, B., Yang, X., & Sun, C. (2024). Principles and applications of convolutional neural network for spectral analysis in food quality evaluation: A review. Journal of Food Composition and Analysis, 105996. https://doi.org/10.1016/j.jfca.2024.105996.

Luo, W., Zhang, J., Huang, H., Peng, W., Gao, Y., Zhan, B., & Zhang, H. (2023). Prediction of fat content in salmon fillets based on hyperspectral imaging and residual attention convolution neural network. LWT, 184, 115018. https://doi.org/10.1016/j.lwt.2023.115018.

Luo, W., Zhang, J., Liu, S., Huang, H., Zhan, B., Fan, G., & Zhang, H. (2024). Prediction of soluble solid content in Nanfeng mandarin by combining hyperspectral imaging and effective wavelength selection. Journal of Food Composition and Analysis, 126, 105939. https://doi.org/10.1016/j.jfca.2023.105939.

Ma, S., Li, Y., & Peng, Y. (2023). Spectroscopy and computer vision techniques for noninvasive analysis of legumes: A review. Computers and Electronics in Agriculture, 206, 107695. https://doi.org/10.1016/j.compag.2023.107695.

Peng, J., Zhang, J., Han, L., Ma, X., Hu, X., Lin, T., ... & Chen, M. (2024). Determination of Malathion Content in Sorghum Grains using Hyperspectral Imaging Technology Combined with Stacked Machine Learning Models. Journal of Food Composition and Analysis, 106635. https://doi.org/10.1016/j.jfca.2024.106635.

Qi, H., Shen, C., Chen, G., Zhang, J., Chen, F., Li, H., & Zhang, C. (2023). Rapid and non-destructive determination of soluble solid content of crown pear by visible/near-infrared spectroscopy with deep learning regression. Journal of Food Composition and Analysis, 123, 105585. https://doi.org/10.1016/j.jfca.2023.105585.

Saha, D., Senthilkumar, T., Sharma, S., Singh, C. B., & Manickavasagan, A. (2023). Application of near-infrared hyperspectral imaging coupled with chemometrics for rapid and non-destructive prediction of protein content in single chickpea seed. Journal of Food Composition and Analysis, 115, 104938. https://doi.org/10.1016/j.jfca.2022.104938.

Saha, D., Senthilkumar, T., Singh, C. B., & Manickavasagan, A. (2023). Quantitative detection of metanil yellow adulteration in chickpea flour using line-scan near-infrared hyperspectral imaging with partial least square regression and one-dimensional convolutional neural network. Journal of Food Composition and Analysis, 120, 105290. https://doi.org/10.1016/j.jfca.2023.105290.

Sato, S., & Numata, Y. (2024). Simultaneous quantitative analysis of quercetin and rutin in Tartary buckwheat flour by Raman spectroscopy and partial least square regression. Journal of Food Composition and Analysis, 128, 105991. https://doi.org/10.1016/j.jfca.2024.105991.

Shuai, L., Li, Z., Chen, Z., Luo, D., & Mu, J. (2024). A research review on deep learning combined with hyperspectral Imaging in multiscale agricultural sensing. Computers and Electronics in Agriculture, 217, 108577. https://doi.org/10.1016/j.compag.2023.108577.

649 Sim, J., Dixit, Y., Mcgoverin, C., Oey, I., Frew, R., Reis, M. M., & Kebede, B. (2024). Machine learning-driven
650 hyperspectral imaging for non-destructive origin verification of green coffee beans across continents, countries, and
651 regions. Food Control, 156, 110159. https://doi.org/10.1016/j.foodcont.2023.110159.

652 Sun, J., Yang, F., Cheng, J., Wang, S., & Fu, L. (2024). Nondestructive identification of soybean protein in minced
653 chicken meat based on hyperspectral imaging and VGG16-SVM. Journal of Food Composition and Analysis, 125,
654 105713. https://doi.org/10.1016/j.jfca.2023.105713.

655 Uebersax, M. A., Cichy, K. A., Gomez, F. E., Porch, T. G., Heitholt, J., Osorno, J. M., ... & Bales, S. (2023). Dry
656 beans (Phaseolus vulgaris L.) as a vital component of sustainable agriculture and food security—A review. Legume
657 science, 5(1), e155. https://doi.org/10.1002/leg3.155.

658 Wainaina, I., Wafula, E., Sila, D., Kyomugasho, C., Grauwet, T., Van Loey, A., & Hendrickx, M. (2021). Thermal
659 treatment of common beans (Phaseolus vulgaris L.): Factors determining cooking time and its consequences for
660 sensory and nutritional quality. Comprehensive Reviews in Food Science and Food Safety, 20(4), 3690-3718.
661 https://doi.org/10.1111/1541-4337.12770.

662 Wang, Y., Wang, S., Yuan, Y., Li, X., Bai, R., Wan, X., ... & Huang, L. (2024). Fast prediction of diverse rare
663 ginsenoside contents in Panax ginseng through hyperspectral imaging assisted with the temporal convolutional
664 network-attention mechanism (TCNA) deep learning. Food Control, 162, 110455.
665 https://doi.org/10.1016/j.foodcont.2024.110455.

666 Yin, H., Xie, B., Chen, B., Ma, J., Chen, J., Zhou, Y., ... & Huang, F. (2023). Detection of moisture content and size
667 of pumpkin seeds based on hyperspectral reflection and transmission imaging techniques. Journal of Food
668 Composition and Analysis, 124, 105651. https://doi.org/10.1016/j.jfca.2023.105651.

669 Yu, D., Lord, N., Polk, J., Dhakal, K., Li, S., Yin, Y., ... & Huang, H. (2022). Physical and chemical properties of
670 edamame during bean development and application of spectroscopy-based machine learning methods to predict
671 optimal harvest time. Food Chemistry, 368, 130799. https://doi.org/10.1016/j.foodchem.2021.130799.

672 Zaukuu, J. L. Z., Nkansah, A. A., Mensah, E. T., Agbolegbe, R. K., & Kovacs, Z. (2024). Non-destructive
673 authentication of melon seed (Cucumeropsis mannii) powder using a pocket-sized near-infrared (NIR)
674 spectrophotometer with multiple spectral preprocessing. Journal of Food Composition and Analysis, 106425.
675 https://doi.org/10.1016/j.jfca.2024.106425.

676 Zhang, J., Guo, Z., Ren, Z., Wang, S., Yin, X., Zhang, D., ... & Ma, C. (2023). A non-destructive determination of
677 protein content in potato flour noodles using near-infrared hyperspectral imaging technology. Infrared Physics &
678 Technology, 130, 104595. https://doi.org/10.1016/j.infrared.2023.104595.

679 Zhang, J., Guo, Z., Ren, Z., Wang, S., Yue, M., Zhang, S., ... & Ma, C. (2023). Rapid determination of protein, starch
680 and moisture content in wheat flour by near-infrared hyperspectral imaging. Journal of Food Composition and
681 Analysis, 117, 105134. https://doi.org/10.1016/j.jfca.2023.105134.

Zhang, S., Yin, Y., Liu, C., Li, J., Sun, X., & Wu, J. (2023). Discrimination of wheat flour grade based on PSO-SVM of hyperspectral technique. Spectrochimica Acta Part A: Molecular and Biomolecular Spectroscopy, 302, 123050. https://doi.org/10.1016/j.saa.2023.123050.

Zhao, Q., Miao, P., Liu, C., Yu, Y., & Li, Z. (2024). Accurate and non-destructive identification of origins for lily using near-infrared hyperspectral imaging combined with machine learning. Journal of Food Composition and Analysis, 129, 106080. https://doi.org/10.1016/j.jfca.2024.106080.

Zhong, H., Chai, J., Yu, C., Wang, K., Wang, K., & Lin, P. (2025). Rapid detection of oil content in Camellia oleifera kernels based on hyperspectral imaging and machine learning. Journal of Food Composition and Analysis, 137, 106899. https://doi.org/10.1016/j.jfca.2024.106899.

a

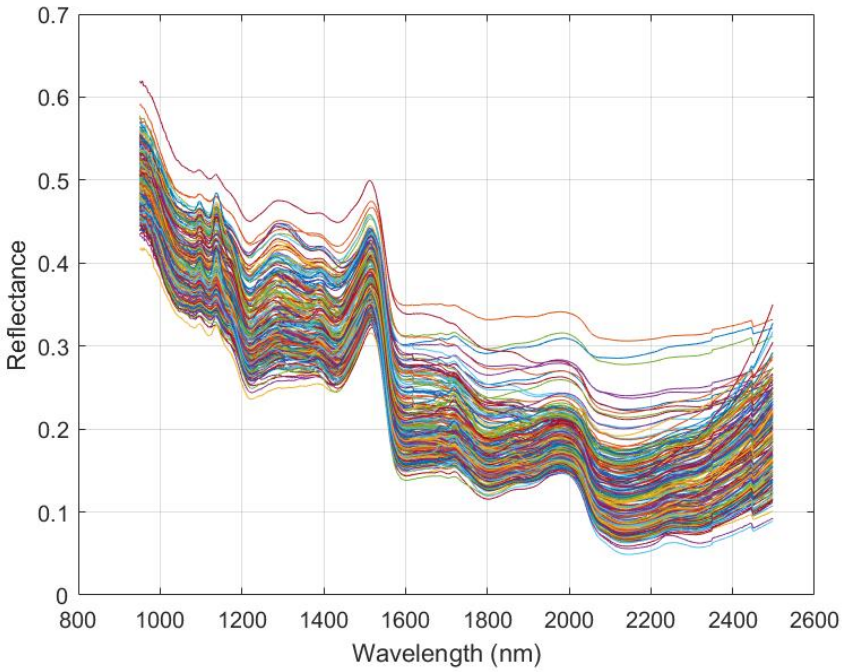
0.7
0.6
0.5
0.4
0.3
0.2
0.1
0
Reflectance
800
1000
1200
1400
1600
1800
2000
2200
2400
2600
Wavelength (nm)

b

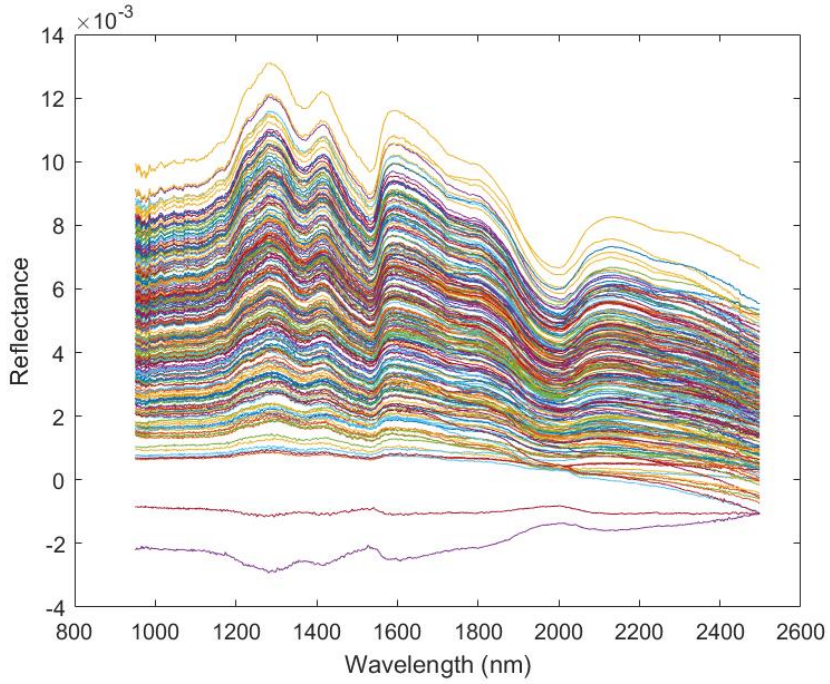
×10-3
14
12
10
8
6
4
2
0
-2
-4
Reflectance
800
1000
1200
1400
1600
1800
2000
2200
2400
2600
Wavelength (nm)

c

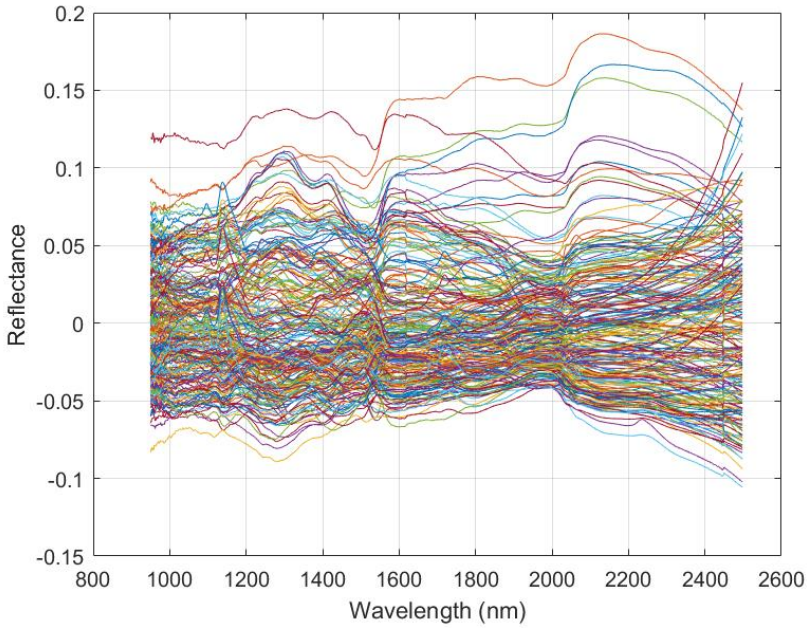
0.2
0.15
0.1
0.05
0
-0.05
-0.1
-0.15
Reflectance
800
1000
1200
1400
1600
1800
2000
2200
2400
2600
Wavelength (nm)

d

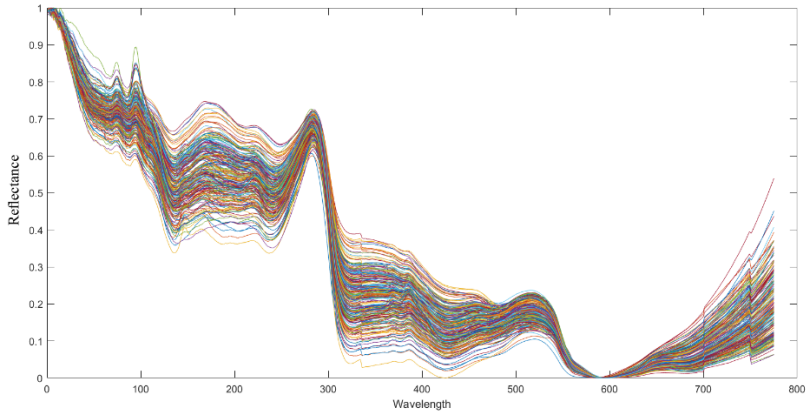
1
0.9
0.8
0.7
0.6
0.5
0.4
0.3
0.2
0.1
0
Reflectance
0
100
200
300
400
500
600
700
800
Wavelength

e

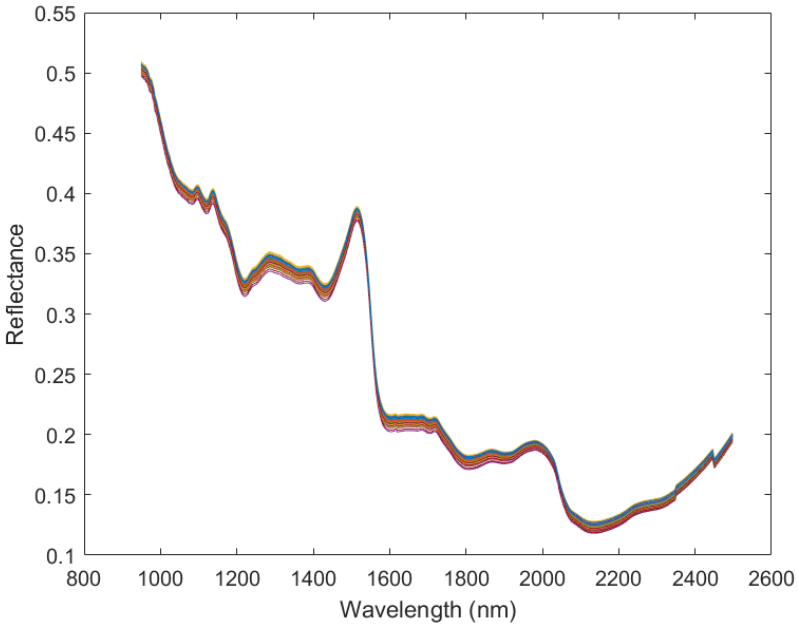
Reflectance
0.55
0.5
0.45
0.4
0.35
0.3
0.25
0.2
0.15
0.1
800
1000
1200
1400
1600
1800
2000
2200
2400
2600
Wavelength (nm)

f

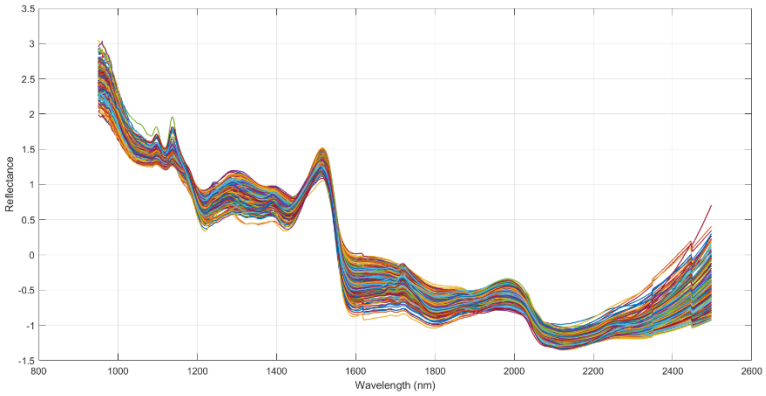
Reflectance
3.5
3
2.5
2
1.5
1
0.5
0
-0.5
-1
-1.5
800
1000
1200
1400
1600
1800
2000
2200
2400
2600
Wavelength (nm)

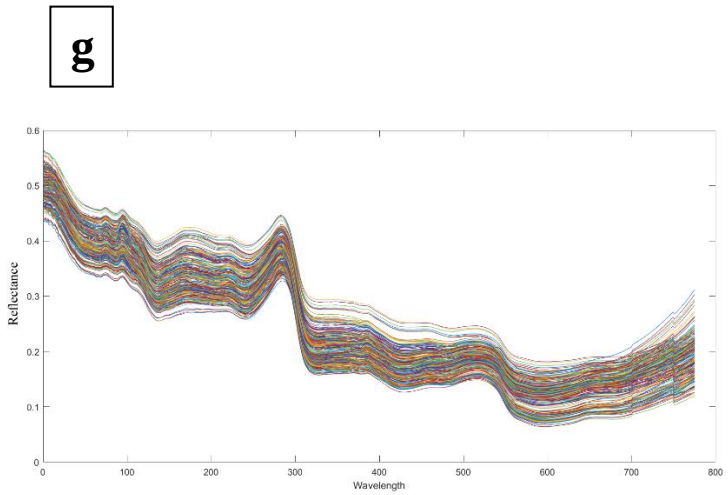

Figure S1. Changes in spectral profiles before and after preprocessing. (a) Original Spectra (b) mean centering (c) probabilistic quotient normalization (d) generalised least squares (e) orthogonal signal correction (f) standard normal variate (g) External parameter orthogonalization

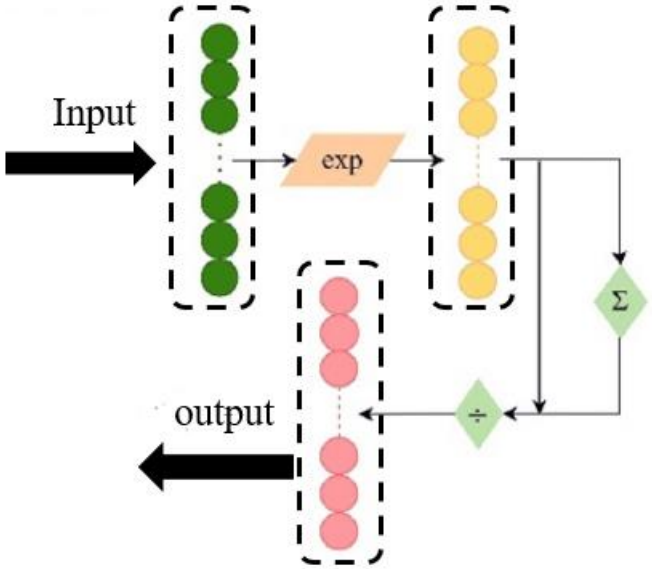

Figure2- The structure of TCNA mechanism in the current research

Table1S. Selection of best kernel for SVMR

Kernel	C	γ	PP	R2
RBF	0.1	0.01	N	0.885
			MC	0.868
			PQN	0.873
			SNV	0.908
			OSC	0.915
			EPO	0.895
			GLS	0.898
		0.1	N	0.886
			MC	0.865
			PQN	0.874
			SNV	0.909
			OSC	0.934
			EPO	0.893
			GLS	0.899
		1	N	0.884
			MC	0.871
			PQN	0.872
			SNV	0.914
			OSC	0.937
			EPO	0.896
			GLS	0.898
	1	0.01	N	0.883
			MC	0.873
			PQN	0.874
			SNV	0.913
			OSC	0.939
			EPO	0.895
			GLS	0.901

		0.1	N	0.882
			MC	0.872
			PQN	0.877
			SNV	0.924
			OSC	0.941
			EPO	0.899
			GLS	0.903
		1	N	0.882
			MC	0.871
			PQN	0.876
			SNV	0.924
			OSC	0.941
			EPO	0.895
			GLS	0.905
	10	0.01	N	0.924
			MC	0.919
			PQN	0.92
			SNV	0.955
			OSC	0.958
			EPO	0.925
			GLS	0.928
		0.1	N	0.881
			MC	0.873
			PQN	0.876
			SNV	0.923
			OSC	0.936
			EPO	0.894
			GLS	0.903
		1	N	0.883

		MC	0.871
		PQN	0.878
		SNV	0.922
		OSC	0.932
		EPO	0.893
		GLS	0.904
Polynomial	0.1	N	0.788
		MC	0.763
		PQN	0.771
		SNV	0.845
		OSC	0.882
		EPO	0.789
		GLS	0.798
	1	N	0.789
		MC	0.765
		PQN	0.772
		SNV	0.855
		OSC	0.887
		EPO	0.792
		GLS	0.792
	10	N	0.787
		MC	0.764
		PQN	0.774
		SNV	0.851
		OSC	0.891
		EPO	0.793
		GLS	0.796
Gaussian		N	0.788
		MC	0.762

Pearson Universal	PQN	0.769
	SNV	0.841
	OSC	0.869
	EPO	0.788
	GLS	0.796
	N	0.785
	MC	0.752
	PQN	0.765
	SNV	0.834
	OSC	0.867
	EPO	0.789
	GLS	0.795